REVISED VERSION

Discovery of moissanite in a peralkaline syenite from the Azores Islands

SABRINA NAZZARENI[A,*], FABRIZIO NESTOLA[B], VITTORIO ZANON[C], LUCA BINDI[D], ENRICO SCRICCIOLO[A], MAURIZIO PETRELLI[A,E], MARCO ZANATTA[F], GINO MARIOTTO[F], GABRIELE GIULI[G]

[a]Dipartimento di Fisica e Geologia, Università di Perugia, Perugia, Italy;

[b]Dipartimento di Geoscienze, Università di Padova, Padova, Italy

[c]Instituto de Investigação em Vulcanologia e Avaliação de Riscos / Universidade dos Açores, Ponta Delgada, Portugal

[d]Dipartimento di Scienze della Terra, Università degli Studi di Firenze, Firenze, Italy

[e] INFN, Perugia, Italy

[f]Dipartimento di Informatica, Università di Verona, Verona, Italy

[g]Scuola di Scienze e Tecnologie – sez. Geologia, Università di Camerino, Camerino, Italy

*Corresponding author: Sabrina Nazzareni (sabrina.nazzareni@unipg.it)

Abstract

Our discovery of moissanite grains in a peralkaline syenite from the Água de Pau Volcano (São Miguel, Azores Islands, Portugal) represents the first report of this mineral in present day oceanic geodynamic settings. Raman spectroscopy and single-crystal X-ray diffraction show the presence of both the 6*H* and 4*H* polytypes with the predominance of the first one. The distribution of trace elements is homogeneous, except for Al and V. Azorean moissanite often hosts rounded inclusions of metallic Si and other not yet identified metallic alloys. A process involving a flushing of CH_4-H_2 ultra-reducing fluids in the alkaline melts might be considered as a possible mechanism leading to the formation of natural SiC, thus calling for strongly reducing conditions that were locally met in the crust-mantle beneath the São Miguel Island.

1. Introduction

Since its discovery in 1893, moissanite (SiC) was recovered in an increasing number of terrestrial tectonic settings: as inclusions in diamonds (Klein-BenDavid et al., 2007), in kimberlites (Marshintsev et al., 1967; Leung et al., 1990; Mathez et al., 1995; Shiryaev et al., 2011), in ophiolites (Trumbull et al., 2009), in granulites and metamorphic rocks (Perraki and Faryad, 2014; Janák et al., 2015; Machev et al., 2018), and in volcanic breccias (Di Pierro et al., 2003; Dobrzhinetskaya et al., 2018). However, despite the increased findings from continental crust sources, moissanite has never been reported from present-day oceanic geodynamic settings.

Doubts often raised on the natural origin of SiC grains because they are commonly recovered in heavy fractions after separation, and only rarely *in situ* (Di Pierro et al., 2003; Dobrzhinetskaya et al., 2018; Machev et al., 2018). Nevertheless, both the morphology and the occurrence/nature of inclusions inside moissanite usually support a natural origin.

The presence of moissanite in such different rocks opened an intense debate to explain its origin (Shiryaev et al., 2011; Di Pierro et al., 2003; Griffin et al., 2016; Dobrzhinetskaya et al., 2018, Machev et al., 2018), mainly because it only forms at extremely reducing conditions, i.e. fO_2 5-7 log units below Iron-Wustite (IW) for mantle conditions (P = 2-10 GPa T = 1000-1700°C; Ulmer et al., 1998; Schmidt et al., 2014). How a silicide (like moissanite) or native elements (like Si^0 or Fe^0)

could coexist with silicates and oxides is still far to be explained.

Moissanite phase diagrams (including polytype stability) applicable to geologically meaningful conditions are scarce and, even when recovered *in situ*, moissanite is never in equilibrium with the coexisting mineral assemblage supporting the idea of its xenocrystic nature.

Here we report discovery of moissanite grains recovered from a concentrated diamagnetic fraction from a peralkaline syenite from the Água de Pau Volcano, at São Miguel (Azores Islands, Portugal). Moissanite has been characterised by micro-Raman spectroscopy (μ-RS), single-crystal X-ray diffraction (SC-XRD) and Laser Ablation Inductively Coupled Plasma Mass Spectrometry (LA-ICP-MS). Beside, inclusions hosted in moissanite were characterized by μ-RS .

2. Geological setting

The Azores region includes nine volcanic islands and several seamounts located in the central-north Atlantic Ocean which constitute the Azores Triple Junction between the Eurasia, Nubia and North America tectonic plates.

Magmatism at the volcano of Água de Pau in São Miguel easternmost island started about 270 ka (Sibrant et al., 2016) with the emission of submarine basalts. The last eruption was in 1563 and involved the formation of a subplinian eruptive column of trachytic pumices. The Holocene activity was dominantly explosive, with two caldera-forming events: Ribeira Chã (8–12 ka BP) and Fogo A (4.6 ka BP) (Wallenstein et al., 2015).

Syenites are relatively common products of this volcano. Three generations of syenite suites have been recognised so far (Widom et al., 1993): they are weakly peralkaline and strongly enriched in trace elements (Ridolfi et al., 2003). The peculiar enrichment determined the formation of REE, Zr and Nb accessory (rare) minerals during late stage of crystallization, in the presence of fluids (Widom et al., 1993).

3. Sample description and methods

78 Samples were collected from the Lombadas ravine, on the northern flank of the volcano. The
79 water stream bed at the bottom of the ravine shows the frequent occurrence of syenite rocks ranging
80 in size from boulders to cobbles. Three texturally different syenites can be found. Metasomatised
81 miarolitic syenite composed mostly of zoned feldspars and acicular amphiboles are rarely found
82 irregularly shaped cobbles. Leucocratic pegmatitic syenite consisting mostly of large perthitic
83 feldspars, plagioclase, biotite and amphibole are frequently found in form of large boulders.
84 Saccaroid-textured medium-grained syenite consisting mostly of sanidine, plagioclase, aegirina-
85 augite, biotite, brown amphibole, apatite, zircon and quartz can be sometimes found as rounded
86 cobbles and pebbles. These rocks host numerous rare REE-bearing minerals the object of the
87 present study. These Syenites are feldspar dominated, with minor amphibole, clinopyroxene, Fe-Ti
88 oxides and quartz (Fig 1), similar to those described by Ridolfi et al. (2003). Accessory minerals are
89 apatite, titanite, eudyalite, aenigmanite, zircon, chevkinite-(Ce), pyrochlore, dalyite, Fe-katophorite,
90 chiappinoite-Y, steacyite, Nb-Zr-bearing astrophillyte and monazite.
91 Syenites were crushed in a steel mortar and then sieved. Diamagnetic component (mainly
92 feldspar, quartz, pyrochlore and zircon) was separated from paramagnetic/ferromagnetic material
93 using a Frantz Isodynamic Magnetic Separator apparatus. Neither further laboratory preparation,
94 nor cutting and polishing treatments on the original syenite were done.
95 About 500 moissanite grains were recovered from 63 gr of the fraction < 0.5 mm of the
96 diamagnetic material (78 gr is the total diamagnetic/para-ferro-magnetic fraction < 0.5 mm). They
97 show deep-blue to green-bluish colours and exhibit a morphology that spans from hexagonal to
98 anhedral.
99 Single-crystal X-ray diffraction was carried out using an Oxford Diffraction Xcalibur
100 diffractometer (X-ray radiation MoKα, $\lambda = 0.71073$ Å) fitted with a CCD detector. After absorption
101 correction reflections data were used for the structural refinement by using SHELXL (Sheldrick,
102 2008). The refinement was done in $P6_3mc$ space group using the atomic coordinates reported by
103 Capitani et al. (2007). The occupancy of all the sites was left free to vary (Si vs. vacancy and C vs.

vacancy) and resulted in a full occupancy by Si and C, respectively. At the last stage, with anisotropic atomic displacement parameters for all atoms and without constraints, the residual value settled at $R1$ = 1.47% for 153 observed reflections [$Fo > 4\sigma(Fo)$ level] and 20 parameters and at $R1$ = 1.83% for all 200 independent reflections.

Micro-Raman measurements were carried out in backscattering geometry using two different instrumentations. A Horiba Jobin-Yvon Labram HR800 spectrometer with a focal length of 800 mm and equipped with a 600 lines/mm grating. The excitation wavelength was the 633 nm line of a He-Ne laser and detected by a CCD detector cooled by liquid nitrogen. Micro-sized regions with a diameter of ~1.5 μm were probed by an 80× long working distance objective. The laser power at the sample surface was ~6 mW and the experimental resolution was about 1.5 cm^{-1}. The second instrument is a Thermo Scientific DXR2 Raman microscope equipped with a long-working distance 50× objective. The excitation source was a 532 nm laser, the spatial resolution 1.1 μm and the minimum spectral resolution was 2.2 cm^{-1}. Un-polarized spectra were collected between 150 and 3570 cm^{-1} in confocal mode through a laser power of 10 mW. The exposure times varied between 5 and 40 s with a 2-5 accumulations per spectrum.

Trace element compositions were estimated by LA-ICP-MS. The instrumentation is a Teledyne Photon Machine G2 laser ablation device, equipped with a two-volume HelEx 2 cell, and coupled to a Thermo Fisher Scientific iCAP Q quadrupole mass spectrometer (Petrelli et al., 2016a). A circular 65 μm spot size, a repetition rate of 8Hz, and a laser fluence of ~3.5 Jcm^{-1} was used. Ablation times were ~50 s per spot, preceded by a 30-s background measurement and followed by 30 s of washout. Data reduction was performed by the Iolite 3 software (Paton et al., 2011). The NIST SRM 610 (Pearce et al., 1997) glass and the USGS BCR2G reference materials were used as calibrator and quality control, respectively. Si was used as internal standard. Under the reported analytical conditions, the precision is better than 10% for concentrations above ~0.1 ppm, and better than 5% above ~2 ppm; accuracy is always better than 10% (Petrelli et al., 2016b).

4. Results

4.1. Crystal structure

Moissanite has a closed packed structure of C (or Si) where the other cation is located in a tetrahedral site. The basic structure is cubic 3*C* polytype (zincblende structure) having the shortest period of repetition of the Si-C layer. The different modes in which this basic layer can repeat along the **c** axis give a unit cell with *n* formula units and is *n* time larger than the basic polytype. The most common polytypes in synthetic material are 4*H* and 6*H* (hexagonal), 15*R* (rhombohedral) and 3*C* (cubic). The 3*C* polytype was found in shocked meteorites and only rarely in terrestrial rocks (Machev et al., 2018); on the other hand, 6*H*, 4*H* and 15*R* were found in kimberlitic, ophiolitic and volcanic rocks (i.e. Di Pierro et al, 2003; Shiryaev et al., 2011, Dobrzhinetskaya et al., 2018).

Hexagonal 6*H* unit-cell parameters were measured by single-crystal X-ray diffraction on three Água de Pau moissanite grains resulting nearly identical. They are very similar to those reported by Capitani et al. (2007) for terrestrial moissanite and those measured for synthetic 6*H*-SiC (RRUFF#R061083, La Fuente et al., 2015). The difference in colour (deep blue and green crystals were measured by SCXRD) is not related to a stabilization of different polytypes but to the presence of peculiar trace elements (Al, B, N) and vacancies (colour centres).

4.2. Raman spectroscopy study

Micro-Raman spectroscopy has been already exploited to discriminate among the different SiC polytypes (i.e. Shiryaev et al., 2011; Dobrzhinetskaya et al., 2018). The presence of strong covalent bonds in SiC leads to a strong Raman scattering of the vibrational modes. Moreover, 4*H* and 6*H* polytypes show characteristic spectra that allow an unambiguous identification. Figure 2 shows a comparison between a typical experimental spectrum acquired on a 6*H* crystal (upper panel) and that obtained on a 4*H* one (lower panel). The positions of the observed modes measured on ca. 40 samples are in good agreement with literature data (Feldman et al., 1968a,b; Nakashima et al., 1997). The identification can be carried out using the low wavenumber planar acoustic modes (see

insets) and the strongest planar optic ones at 790 cm^{-1} (6*H*-SiC) and 777 cm^{-1} (4*H*-SiC). It is worth mentioning that, in addition to relative peak intensity effects, due to polarization, the position of some modes in SiC polytypes also shows a dependence on the angle between the direction of the incident laser beam and the crystal *c*-axis (Feldman et al., 1968a,b). In particular, this is true for the peaks occurring in the region between 750 cm^{-1} and 1000 cm^{-1}, with the notable exception of the mode at about 797 cm^{-1}, which is angle and polytype independent.

Inclusions with unusual composition (metallic Si, Mg-, Cr-, Ti-, Fe-silicides, silicon oxy-carbides, tistarite, CAS minerals, Fe-Ti-Si-C-P metallic alloys) are reported in natural moissanite (Marshintsev et al., 1967; Mathez et al., 1995; Di Pierro et al., 2003; Shiryaev et al., 2011; Griffin et al., 2016; Dobrzhinetskaya et al., 2018). A detailed characterization of the inclusions could provide constrains about SiC crystallisation in terms of fO_2, related fluids and ultimately on the crystallization pressure as already achieved for diamonds (i.e. Anzolini et al., 2018; Nestola et al., 2018).

In Azorean moissanite we identified at least two types of nanometric to micrometric (< 40 microns) inclusions: 1) elongated transparent, 2) round-shaped dark (Fig. 3). The inclusions of type 1 did not provide any Raman signals and were not identified; on the contrary, spectra of type 2 inclusions show a strong peak at ~520 cm^{-1} not belonging to the 6*H* host moissanite (Fig. 3). Even if we did not release the inclusions, we are confident that it can be identified as Si^0. We have compared the Raman shift of the Si^0 inclusion band at about 520 cm^{-1} with respect to the position of the same band measured for a synthetic Si^0 using the same instrumentation during the same Raman session.

The band position of the synthetic Si^0 measured in this work is at 520.72 cm^{-1} with a full width half maximum (FWHM) equal to 7.06 cm^{-1}; the band position of our Si^0 inclusion is positioned at 519.65 cm^{-1} with a FWHM totally comparable to the synthetic one (i.e. 6.07 cm^{-1}) . Based on Weinstein and Piermarini (1975) Raman calibration performed on Si^0, such Raman band variation would correspond to a negative residual pressure P_{inc} = 0.2 GPa (see Anzolini et al., 2018 and

Nestola et al., 2018 for more details about the P_{inc}). From the residual pressure and knowing the thermoelastic properties of host and inclusion, we can back-calculate the depth of formation. For example, a residual pressure of 0.2 GPa for a kyanite inclusion within a diamond provides a pressure of about 5.3 GPa at T = 1120°C (Nestola et al., 2018). However, in case of the moissanite-Si^0 host-inclusion system, our data is providing a negative residual pressure, meaning that the inclusion is stretched. To explain such behavior, we can use the yield strength of moissanite, which was determined up to 18.3 GPa and 1200 °C by Zhang et al. (2002). At the maximum temperature reached by the authors, the yield strength of moissanite is 4.2 GPa, at the same temperature the yield strength of diamond is about 13 GPa (Weidener et al., 1994), which means that diamond has a much bigger resistance to the plastic deformation. Therefore, during exhumation to the surface at high temperature the moissanite host, and as a consequence, the cavity around the Si^0 inclusion, may have undergone a plastic expansion in addition to the elastic deformation, resulting in a stretched inclusion with negative P_{inc} at retrieval. Therefore, the application of a purely elastic geobarometry approach (see Nestola et al., 2011) to such inclusions may lead to wrong estimate of the initial conditions of entrapment.

4.3. Trace element distribution

A general low content of trace elements was measured in 16 moissanite samples (Table 1 APPENDIX), confirming what already observed in moissanite from kimberlite (Shiryaev et al., 2011). The few trace elements measured above the detection limits in Azorean moissanite are B, Sc, Ti, Al and V. They have a quite homogeneous distribution with values of B = 1.8 - 6.6 ppm (average 4.4 ppm), Sc = 15.5 - 17.2 ppm (average 16.2 ppm), Ti = 10.5 - 26 ppm (average 14.1 ppm). The higher variability was observed for vanadium (from 0.2 to 17 ppm) and aluminium (from 190 to 1415 ppm) contents.

As reported by Shiryaev et al. (2011) even synthetic SiC has very few trace elements content that overlaps the values of natural samples. They observed that moissanite, like diamond, is able to host

only atoms that can substitute Si (or C) in its structure like Al, N, B, and that most of the trace elements partition preferentially into the syngenetic inclusions (alloys, carbides and silicides). Although low, the trace elements content in kimberlitic SiC shows some variability (see Mir vs Udachnaya SiC in Shiryaev et al., 2011), and show lower B, Al, Ti and V values than the Azorean samples whereas the Sc content is similar to Aikhal SiC (Shiryaev et al., 2011).

The scarcity of trace elements data on moissanite and its inclusions from different rock types prevents any deep geochemical considerations.

4. Discussion and conclusions

Two main questions must be addressed: where the Azorean moissanite originated, and how the remarkably reduced conditions were achieved in the environment. Several models have been proposed to explain how natural SiC could occur under extremely different geological settings, especially whether it has or not a mantle origin (i.e., Mathez et al., 1995; Ulmer et al., 1998; Rogers et al., 1989; Schmidt et al., 2014; Shiryaev and Gaillard, 2014; Griffin et al., 2018; Ballhaus et al., 2018). Common point of these models is the very low oxygen fugacity (fO_2 = 7–5 log units below the IW buffer) and high temperature (from 700°C to 2500°C).

The current models are related to experiments in the peridotitic system (Ulmer et al., 1998; Schmidt et al., 2014) or to thermodynamic calculations (Mathez et al., 1995; Shiryaev and Gaillard, 2014). These models also suggest that these conditions could occur locally, even at the grain scale, since the redox conditions at mantle or crustal conditions are usually oxidising (QFM-buffered).

Ultra-reducing C-O-H fluids were invoked to obtain such an environment that stabilizes SiC and metallic alloys (Schmidt et al., 2014; Griffin et al., 2018; Dobrzhinetskaya et al., 2018). Such reducing C-O-H fluids can be obtained for example by change the H/O ratio as a result of H_2O subtraction, at carbon saturated conditions, moving the isopleths towards CH_4-rich fluid, without changing fO_2 (Schmidt et al., 2014). At low pressure during magma ascent, decompression can

trigger redox reactions in carbon-saturated melt with high-silica activity to form moissanite at around 1300°C (Shiryaev and Gaillard, 2014). Griffin et al. (2018) suggested a worldwide process in which reduced C-O-H-N fluids may be transported from deep Earth up to at least the base of the lithosphere and, depending on its thickness, different redox reactions can be triggered (i.e., with diamond or SiC formation). Mt. Carmel moissanite formation is based on this model: mantle-derived fluids dominated by $CH_4 + H_2$ interacted with an alkaline basalt melt at 60-100 km (2-3 GPa) depth and 1000 °C ≥ T ≤ 1660 °C (Griffin et al., 2018; Dobrzhinetskaya et al., 2018). Nevertheless, there are no evidences of CH_4 dominant fluids in ol and cpx-hosted fluid inclusions at the Azores (Zanon and Frezzotti, 2014; Métrich et al., 2015; Zanon, 2015).

We recovered ca. 500 moissanite grains in 78 gr. of fine-grained (<0.5 mm) syenite, lacking textural information. However, the mineral assemblage of the syenite (feld, ± amph, cpx, ann, Fe-Ti oxides and sodalite or quartz) cannot be in equilibrium with extremely reduced phase like SiC or metallic Si. The Água de Pau syenites are characterised by a wealth of accessory minerals enriched in REE, Zr, and Nb are the ultimate stage of crystallisation of a trachyte (Ridofi et al., 2003). Even if during this late stage of the chemical evolution a decrease in fO_2 has been proposed (Ridolfi et al., 2003), it seems very unlikely that fO_2 reached the extremely reduced conditions requested for the SiC formation. Moreover, SiC is not stable together with Fe-rich minerals like those occurring as accessory in the Água de Pau syenite.

Azorean moissanites are 90% the 6*H* polytype, suggesting that they grew at similar *P-T* conditions and degree of impurities, and that no polytype transformation occurred since their formation. The presence of Si^0 inclusions supports the natural origin of these grains but currently it does not provide any indication of pressure as the actual depth of formation was somehow reset to the H*T*-L*P* conditions typical of the syenite crystallization. In case of moissanite and its inclusions, it is not trivial to apply the elastic geobarometry approach unless the crystal is erupted rapidly from H*P* conditions like happens for the typical kimberlitic magmas. In order to prove such hypothesis, a systematic study of inclusions present in the Azorean and in kimberlitic moissanites is currently

256 under progress, aiming at applying the elastic geobarometry to all typologies of inclusions.
257 However, such approach requires a complete revision of all thermodynamic parameters for host and
258 inclusion, information not at moment available for many inclusions found in moissanite.

259 Furthermore, without considering the influence of pressure, assuming that Si metal was
260 entrapped as a liquid phase by moissanite, a temperature of ~1400°C (melting point for Si^0) was
261 needed. Actually, the temperature of evolved liquids at São Miguel is ~730-780 °C (Renzulli and
262 Santi, 2000), whereas São Miguel basalts are originated at ≈ 3-4 GPa and T ≈ 1300°C-1400°C
263 (Beier et al., 2008).

264 Hardly we can directly apply the current models to explain the formation of Azorean moissanite.
265 Azores Islands are located in oceanic extensional setting; nevertheless, the enriched geochemical
266 signature of the São Miguel magmas likely derives from the recycle of an old (≈3 Ga) crustal
267 component into the mantle (Béguelin et al., 2017; Schaefer et al., 2002).

268 Even if we lack textural information, starting from the point that moissanite is not a phase that
269 normally crystallises in syenitic melts, we may hypothesise that our grains were formed by ultra-
270 reducing (metasomatic/hydrothermal) fluids possibly reacting with the alkaline melt at some stage
271 of the syenite formation/emplacement. The current data cannot solve whether this process occurred
272 when alkaline magma formed by partial melting in the lithosphere or at some stage between the
273 formation and ascent to the magma chamber.

274 A more detailed study of inclusions and the recovery of *in situ* moissanite would help to convey
275 on a more reliable model. As far as we know, this is the first report of moissanite in a non-
276 continental geodynamic settings, widening the tectonic settings where SiC occurred.

277

278

279 **Acknowledgments**

280 This study was partially funded by Fundação para a Ciência e Tecnologia, Portugal (MARES
281 project PTDC/GEO-FIQ/1088/2014). FN thanks the European Research Council for funding the

282 research (agreement n. 307322). Editor Marco Scambelluri, Larissa Dobrzhinetskaya and an
283 anonymous reviewer are greatly acknowledged for their constructive comments and suggestions.
284

Figure and Table captions

Figure 1. Microphotograph of a typical saccaroid-textured syenite, showing the presence of sanidine, two amphiboles, apatite, quartz, pyroxene and aenigmatite.

Figure 2. Typical micro-Raman spectra of 6*H* (upper panel) and 4*H* (lower panel) polytypes. Insets: insight of the low wavenumber region; peaks position of 6*H*-SiC is 236 cm^{-1}, 242 cm^{-1} and 267 cm^{-1} peaks position of 4*H*-SiC is 196 cm^{-1} and 204 cm^{-1}. The uncertainness on the peak positions is ±1 cm^{-1}.

Figure 3. Analysis of two typical Si^0 inclusions enclosed in *6H*-SiC crystals (A1 and A2). From left to right: low magnification image of the crystal with the inclusion, high-magnification detail of the inclusion, and μRS spectrum acquired on the inclusion. The Si^0 peak at 520 cm^{-1} is marked with a red arrow.

Appendix material

Table 1. Trace elements composition of moissanite crystals.

306 References

307 Anzolini, C., Prencipe, M., Alvaro, M., Romano, C., Vona, A., Lorenzon, S., Smith, E.M., Brenker,
308 F.E., Nestola, F. (2018) Depth of formation of super-deep diamonds: Raman barometry of $CaSiO_3$-
309 walstromite inclusions. American Mineralogist, 103, 69-74.

310 Ballhaus, C., Wirth, R., Fonseca, R.O.C., Blanchard, H., Pröll, W., Bragagni, A., Nagel, T.,
311 Schreiber, A., Dittrich, S., Thome, V., Hezel, D.C., Below, R., Cieszynski, H., 2017. Ultra-high
312 pressure and ultra-reduced minerals in ophiolites may form by lightning strikes. Geochemical
313 Perspective Letters 5, 42–46.

314 Béguelin, P., Bizimis, M., Beier, C., Turner, S., 2017. Rift–plume interaction reveals multiple
315 generations of recycled oceanic crust in Azores lavas. Geochimica Cosmochimica Acta 218, 132-
316 152.

317 Beier, C., Haase, K.M., Abouchami, W., Krienitz, M.-S., Hauff, F., 2008. Magma genesis by rifting
318 of oceanic lithosphere above anomalous mantle: Terceira Rift, Azores. Geochemistry, Geophysics,
319 Geosystems 9, Q12013.

320 Capitani, G.C., Di Pierro, S., Tempesta, G., 2007. The 6H-SiC structure model: Further refinement
321 from SCXRD data from a terrestrial moissanite. American Mineralogist 92, 403–407.

322 Di Pierro, S., Gnos, E., Grobety, B.H., Armbruster, T., Bernasconi, S.M., Ulmer, P., 2003. Rock-
323 forming moissanite (natural α-silicon carbide). American Mineralogist 88, 1817–1821.

324 Dobrzhinetskaya L, Mukhin P, Wang Q., Wirth R., O'Bannon E., Zhao W., Eppelbaum L.,
325 Sokhonchuk T., 2018. Moissanite (SiC) with metal-silicide and silicon inclusions from tuff of
326 Israel: Raman spectroscopy and electron microscope studies. Lithos 310-311, 355-368.

327 Feldman, D.W., Parker Jr., J.H., Choyke,W.J., Patrick, L., 1968a. Raman Scattering in 6H SiC.
328 Physical Review 170, 698-704.

329 Feldman, D.W., Parker Jr., J.H., Choyke,W.J., Patrick, L., 1968b. Phonon dispersion curves by
330 Raman scattering in SiC, polytypes 3C, 4H, 6H, 15R, and 21R. Physical Review 173, 787–793.

331 Griffin, W. L., Huang, J-X., Thomassot, E., Gain, S. E. M., Toledo V., O'Reilly, S. Y., 2018.
332 Super-reducing conditions in ancient and modern volcanic systems: sources and behaviour of
333 carbon-rich fluids in the lithospheric mantle. Mineralogy and Petrology
334 https://doi.org/10.1007/s00710-018-0575-x.

335 Griffin, W.L., Gain, S.E.M., Adams, D.T., Huang, J-X., Saunders, M., Toledo, V., Pearson, N.J.,
336 O'Reilly, S.Y., 2016. First terrestrial occurrence of tistarite (Ti2O3): ultra-low oxygen fugacity in
337 the upper mantle be- neath Mt. Carmel, Israel. Geology, 44, 815–818.

338 Janák, M., Froitzheim, N., Yoshida, K., Sasinková, V., Nosko, M., Kobayashi, T., Hirajima, T.,
339 Vrabec, M., 2015. Diamond in metasedimentary crustal rocks from Pohorje, Eastern Alps: a
340 window to deep continental subduction. Journal of Metamorphic Geology 33, 495–512.

341 Klein-BenDavid, O., Wirth, R., Navon, O., 2007. Micrometer-scale cavities in fibrous and cloudy
342 diamonds — a glance into diamond dissolution events. Earth and Planetary Science Letters 264,
343 89–103.\l

344 Lafuente, B., Downs, R.T., Yang, H., Stone, N. 2015. The power of databases: the RRUFF project.
345 In: Highlights in Mineralogical Crystallography, T Armbruster and R M Danisi, eds. Berlin,
346 Germany, W. De Gruyter, pp 1-30.

347 Leung, I., Guo, W., Freidman, I., Gleason, J., 1990. Natural occurrence of silicon carbide in a
348 diamondiferous kimberlite from Fuxian. Nature 346, 352–354.

349 Machev, P., O'Bannon, E.F., Bozhilov, K.N., Wang, Q., Dobrzhinetskaya, L., 2018. Not all
350 moissanites are created equal: New constraints on moissanite from metamorphic rocks of Bulgaria.
351 Earth and Planetary Science Letters 498, 387–396.

352 Marshintsev, V.K., Shchelchkova, S.G., Zol'nikov, G.V., Voskresenskaya, V.B., 1967. New data on
353 moissanite from the Yakutian kimberlites. Geologiya i Geofizika 12, 22–31.

354 Mathez, E.A., Fogel, R.A., Hutcheon, I.D., Marshintsev, V.K., 1995. Carbon isotopic composition
355 and origin of SiC from kimberlites of Yakutia, Russia. Geochimica et Cosmochimica Acta, 59,

781–791.

Métrich, N., Zanon, V., Créon, L., Hildenbrand, A., Moreira, M., Marques, F.O., 2015. Is the "Azores hotspot" a wetspot? Insights from the geochemistry of the fluid and melt inclusions in olivines of Pico basalts. Journal of Petrology 55(2), 377-393.

Nakashima, S., Harita, H., 1997. Raman investigation of SiC polytypes. Physica Status Solidi A162, 39–64.

Nestola, F., Nimis, P., Ziberna, L., Longo, M., Marzoli, A., Harris, J.W., Manghnani, M.H., Fedortchouk, Y., 2011. First crystal-structure determination of olivine in diamond: Composition and implications for provenance in the Earth's mantle. Earth and Planetary Science Letters, 305, 249-255.

Nestola, F., Prencipe, M., Nimis, P., Sgreva, N., Perritt, S.H., Chinn, I.L., Zaffiro, G., 2018. Toward a robust elastic geobarometry of kyanite inclusions in eclogitic diamonds. Journal of Geophysical Research – Solid Earth, 123, 6411-6423.

Paton C., Hellstrom J., Paul B.,Woodhead J., Hergt J., 2011. Iolite: Freeware for the visualisation and processing of mass spectrometric data. Journal of Analytical Atomic Spectrometry 26, 2508-2518.

Pearce J.G.N., Perkins W.T., Westgate J.A., Gorton M.P., Jackson S.E., Neal C.R., Chenery S.P., 1997. A compilation of new and published major and trace element data for NIST SRM 610 and NIST SRM 612 glass reference materials. Geostandards Newsletter 21, 115-144.

Perraki, M., Faryad, S.W., 2014. First finding of microdiamond, coesite and other UHP phases in felsic granulites in the Moldanubian Zone: implications for deep subduction and a revised geodynamic model for Variscan Orogeny in the Bohemian Massif. Lithos 202, 157–166.

Petrelli, M., Laeger, K., Perugini, D., 2016a. High spatial resolution trace element determination of geological samples by laser ablation quadrupole plasma mass spectrometry: Implications for glass analysis in volcanic products. Geosciences Journal, 20, 1–13.

Petrelli, M., Morgavi, D., Vetere, F., Perugia, D., 2016b. Elemental imaging and petro-volcanological applications of an improved Laser Ablation Inductively Coupled Quadrupole Plasma Mass Spectrometry. Periodico di Mineralogia 85(1), 25-39.

Renzulli, A., Santi, P., 2000. Two stage fractionation history of the alkali basalt-trachyte series of Sete Cidades volcano (São Miguel Island, Azores). Europran Journal of Mineralogy. 12(2), 469-494.

Ridolfi, F,. Renzulli, A,. Santi, P., Upton, B.G.J., 2003. Evolutionary stages of crystallization of weakly perlakaline syenite: evidence from ejecta in the plinian deposits of Agua de Pau volcano (São Miguel Azores Islands) .Mineralogical Magazine, 67(4), 749-767.

Rogers K.A, Courtney S.F. Seelye R., McCulloch B.A., Mulholland I. (1989) An occurrence of "moissanite" (SiC) from seddonville, west coast, New Zealand. New Zealand Natural Sciences 16, 105-108.

Schaefer, B.F., Turner, S., Parkinson, I., Rogers, N., Hawkesworth, C., 2002. Evidence for recycled Archaean oceanic mantle lithosphere in the Azores plume. Nature 420, 304-307.

Schmidt M.W., Gao G., Golubkova, A., Rohrbach, A., Connolly, J.A.D., 2014. Natural moissanite (SiC) – a low temperature mineral formed from highly fractionated ultra-reducing COH-fluids. Progress in Earth and Planetary Science 2014, 1-27.

Sheldrick, G.M., 2008. A short history of SHELX. Acta Crystallographica A64, 112–122.

Shiryaev A.A., Gaillard, F., 2014. Local redox buffering by carbon at low pressures and the formation of moissanite – natural SiC. European Journal of Minerals, 26(1), 53-59.

Shiryaev, A.A., Griffin, W.L. Stoyanov, E., 2011. Moissanite (SiC) from kimberlites: Polytypes, trace elements, inclusions and speculations on origin. Lithos 122, 152–164.

Sibrant, A.L.R., Marques, F.O., Hildenbrand, A., Boulesteix, T., Costa, A.C.G., Catalão, J., 2016. Deformation in a hyper-slow oceanic rift: insights from the tectonics of the S. Miguel Island (Terceira Rift, Azores). Tectonics 35(2), 425–446.

Trumbull, R.B., Yang, J.-S., Robinson, P.T., Di Pierro, S., Vennemann, T., Wiedenbeck, M., 2009. The carbon isotope composition of natural SiC (moissanite) from the Earth's mantle: new discoveries from ophiolites. Lithos 113, 612–620.

Ulmer, G.C., Grandstaff, D.E., Woermann, E., Gobbels, M., Schonitz, M., Woodland, A.B., 1998. The redox stability of moissanite (SiC) compared with metal-metal oxide buffers at 1773 K and at pressures up to 90 kbar. Neues Jahrbuch Mineralogie, Abhandlungen 172, 279–307.

Wallenstein, N., Duncan, A.M., Guest, J.E., Almeida, M.H., 2015. Eruptive history of Fogo Volcano, São Miguel, Azores. In: Gaspar JL, Guest JE, Duncan AM, Barriga FJAS, Chester DK (eds) Volcanic Geology of São Miguel Island (Azores Archipelago). Geological Society, London, Memoirs, pp 105–123

Weidener, D.J., Wang, Y., Vaughan, M.T., 1994. Strength of diamond. Science, 266, 419-422.

Weinstein, T., Piermarini, G.J., 1975. Raman scattering and phonon dispersion in Si and GaP at very high pressure. Physical Review B, 12, number 4.

Widom, E., Gill, J.B., Schmincke, H.U., 1993. Syenite nodules as long term record of magmatic activity in Agua de Pau Volcano, Sao Miguel, Azores. Journal of Petrology, 34, 929-953.

Zanon, V., 2015**.** Conditions for mafic magma storage beneath fissure zones at oceanic islands. The case of São Miguel island (Azores archipelago). In Caricchi L & Blundy J.D. (eds) Chemical, physical and temporal evolution of magmatic systems. Geological Society of London, special publication, 442, 85-104.

Zanon, V., Frezzotti, M.L., 2013. Magma storage and ascent conditions beneath Pico and Faial islands (Azores Islands). A study on fluid inclusions. Geochemistry, Geophysics, Geosystems 14 (9), 3494–3514.

428 Zhang, J. Wang L., Weidner D.J., Uchida, T., Xu J-A., 2002. The strength of moissanite. American
429 Mineralogist 87(7) 1005-1008.

430

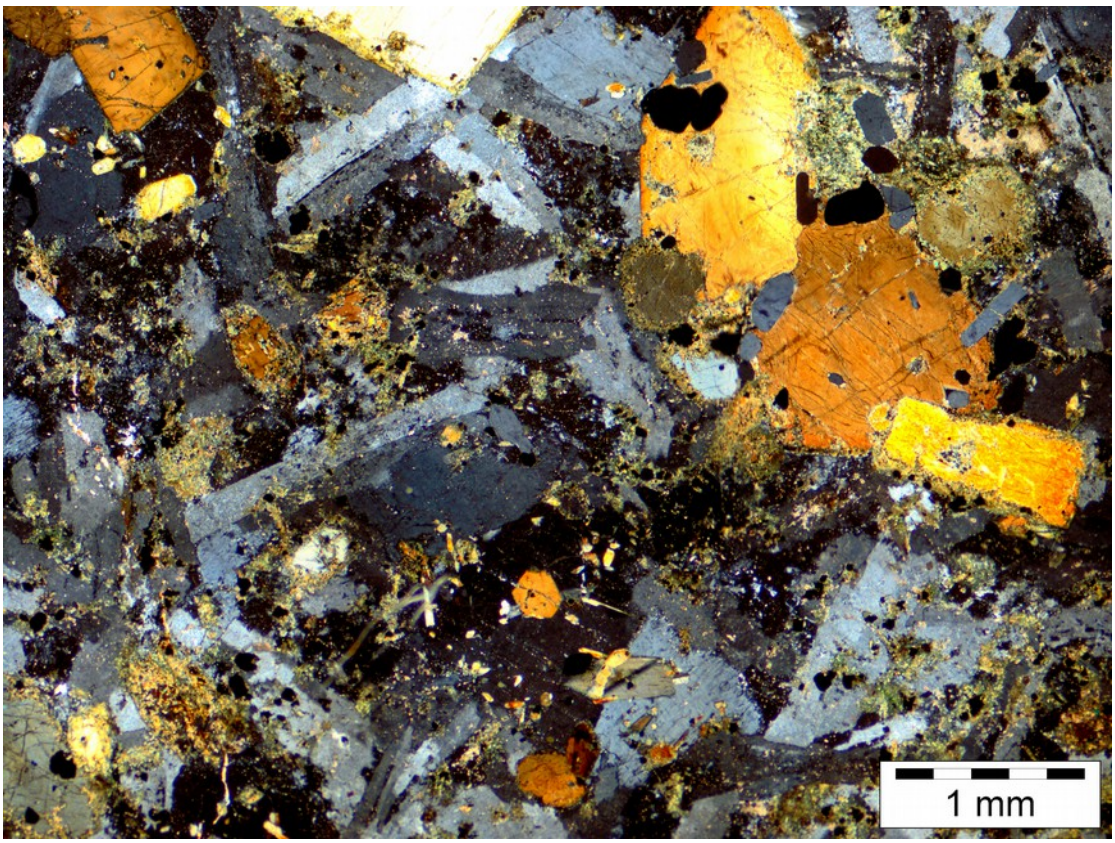
1 mm

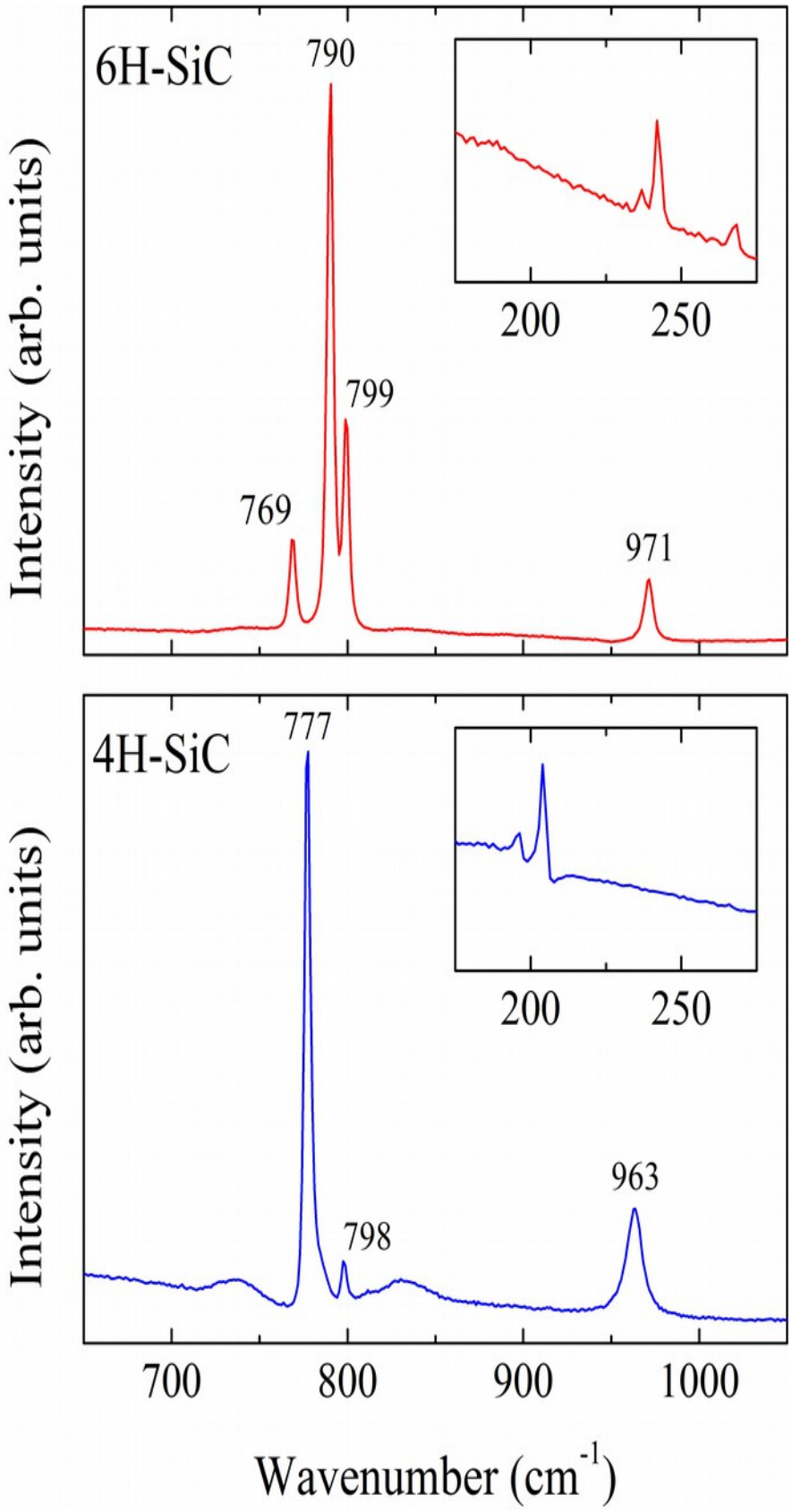
6H-SiC
790
799
769
971
200
250
Intensity (arb. units)
4H-SiC
777
798
963
200
250
Intensity (arb. units)
700
800
900
1000
Wavenumber (cm-1)

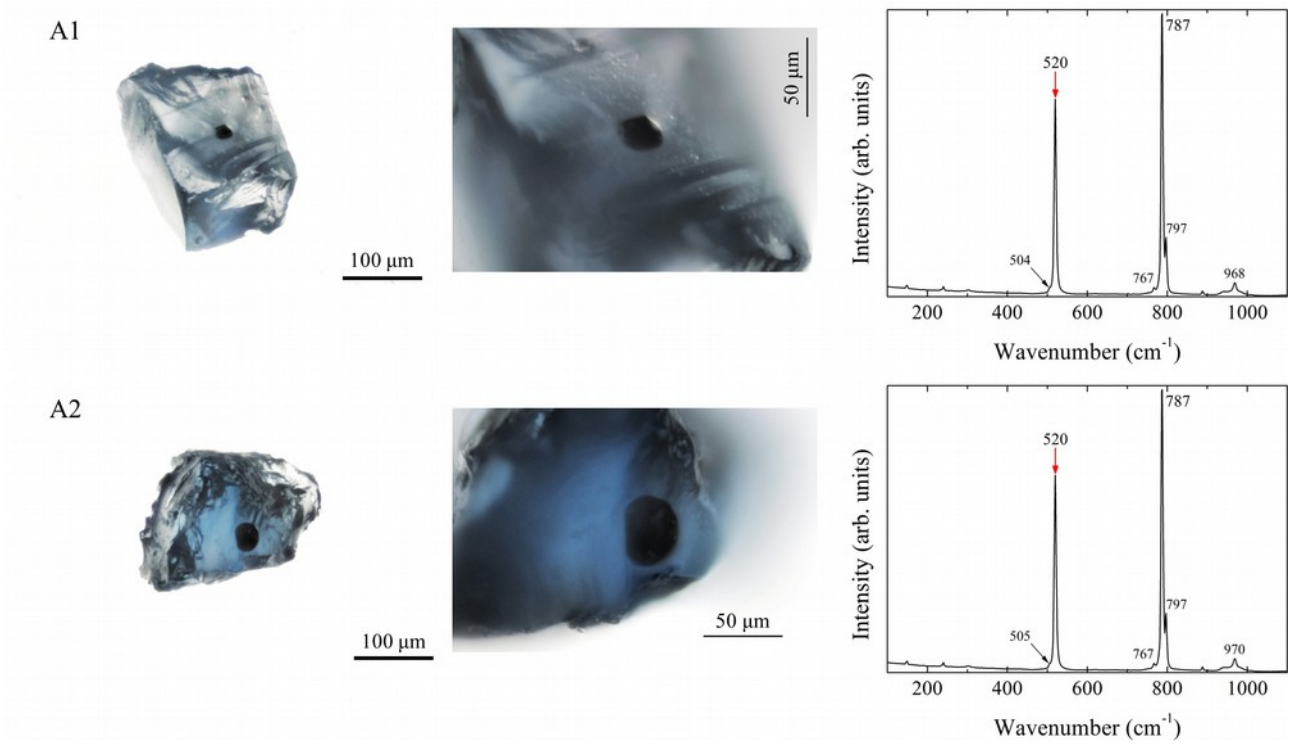
A1
100 µm
50 µm
787
520
797
504
767
968
200
400
600
800
1000
Intensity (arb. units)
Wavenumber (cm-1)
A2
100 µm
50 µm
787
520
797
505
767
970
200
400
600
800
1000
Intensity (arb. units)
Wavenumber (cm-1)

434

435

Table 1

	SiC_146		SiC_147		SiC_148		SiC_149		SiC_150		SiC_151		SiC_152		SiC_153	
	µg/g	2s	µg/g	2s	µg/g	2s	µg/g	2s	µg/g	2s	µg/g	2s	µg/g	2s	µg/g	2s
B	-	-	1.8	0.7	4.1	0.7	6.5	0.8	6.6	1.5	3.6	0.7	5.6	0.7	5.6	1.2
Al	270	9	453	14	345	7.8	192	6.4	1106	43	256	8.8	445	18	304	11
Sc	16	0.5	17	0.7	16	0.5	16	0.6	16	0.7	16	0.6	16	1.1	16	0.7
Ti	11	1.1	11	0.9	12	1.2	15	1.3	27	2.8	10	1	15	1.6	16	1.4
V	0.4	0.06	0.9	0.1	3.6	0.2	8.6	0.3	18	0.78	0.22	0.06	5.4	0.3	6.7	0.3
Cr	-	-	-	-	0.83	0.55	-	-	-	-	-	-	-	-	-	-
Zn	0.64	0.55	-	-	0.29	0.16	0.52	0.21	0.64	0.36	1	1.3	0.42	0.19	0.86	0.73
Ga	-	-	-	-	-	-	-	-	-	-	-	-	-	-	-	-
Sr	-	-	-	-	-	-	-	-	-	-	-	-	-	-	-	-
Zr	-	-	-	-	-	-	-	-	-	-	-	-	-	-	-	-
Nb	-	-	-	-	-	-	-	-	-	-	-	-	-		-	-
Mo	-	-	-	-	-	-	-	-	-	-	-	-	-		-	-
Sn	0.18	0.05	0.16	0.05	0.21	0.05	0.21	0.05	0.18	0.07	0.15	0.04	0.13	0.06	0.19	0.10
Ba	-	-	-	-	-	-	-	-	-	-	-	-	-	-	-	-
Ce	-	-	-	-	-	-	-	-	-	-	-	-	-	-	-	-
Eu	-	-	-	-	-	-	-	-	-	-	-	-	-	-	-	-
Tm	-	-	-	-	-	-	-	-	-	-	-	-	-	-	-	-
Hf	-	-	-	-	-	-	-	-	-	-	-	-	-	-	-	-
Ta	-	-	-	-	-	-	-	-	-	-	-	-	-	-	-	-
Pb	0.038	0.018	-	-	0.17	0.28	0.03	0.01	0.047	0.028	0.09	0.1	-	-	-	-
U	-	-	-	-	-	-	-	-	-	-	-	-	-	-	-	-

437

Table 1

SiC_154		SiC_155		SiC_156		SiC_157		SiC_158		SiC_159		SiC_160		average	st. dev.	d. l.
µg/g	2s	µg/g	2s	µg/g	2s	µg/g	2s	µg/g	2s	µg/g	2s	µg/g	2s	µg/g		µg/g
2.8	0.6	2.0	0.5	5.3	0.8	6.4	0.8	2.1	0.6	-		4.4	1.3	4.4	1.8	1
1237	36	581	18	179	4.4	198	5.2	751	19	1415	33	201	6.4	529	411	0.8
16	0.6	16	0.6	16	0.6	16	0.5	16	0.6	16	0.5	16	0.8	16.2	0.4	0.2
16	1.3	10	0.9	14	1.2	23	1.5	10	0.9	11	1.1	11	1.6	14	5	1
5.3	0.3	0.45	0.18	6.9	0.3	17	0.4	0.47	0.07	0.36	0.06	1.9	0.2	5	6	0.1
1.2	0.6	-	-	-	-	-	-	-	-	-	-	-	-	-	-	0.6
0.28	0.16	-	-	0.38	0.17	0.35	0.21	0.67	0.41		-	0.67	0.29	0.6	0.2	0.3
-	-	-	-	-	-	-		-	-	-	-	-	-	-	-	0.02
-	-	-	-	-	-	-		-	-	-	-	-	-	-	-	0.005
-	-	-	-	-	-	-	0.023	-	-	-	-	-	-	-	-	0.01
-	-	-	-	-	-	-		-	-	-	-	-	-	-	-	0.006
-	-	-	-	-	-	-		-	-	-	-	-	-	-	-	0.06
0.10	0.03	0.14	0.05	0.16	0.04	0.19	0.038	0.16	0.05	0.14	0.05	0.14	0.07	0.16	0.03	0.08
-	-	-	-	-	-	-	-	-	-	-	-	-	-	-	-	0.02
-	-	-	-	-	-	-	-	-	-	-	-	-	-	-	-	0.003
-	-	-	-	-	-	-	-	-	-	-	-	-	-	-	-	0.004
-	-	-	-	-	-	-	-	-	-	-	-	-	-	-	-	0.002
-	-	-	-	-	-	-	-	-	-	-	-	-	-	-	-	0.008
-	-	-	-	-	-	-	-	-	-	-	-	-	-	-	-	0.002
0.034	0.015	-	-	0.023	0.012	0.037	0.017	0.037	0.044	-	-	0.09	0.053	0.060	0.05	0.02
-	-	-	-	-	-	-	-	-	-	-	-	-	-			0.003

439